Ballistic to Diffusive Crossover in III–V Nanowire Transistors

M. J. Gilbert, *Member, IEEE*, and Sanjay K. Banerjee, *Fellow, IEEE*

***Abstract*—In this paper, we examine the crossover between ballistic and diffusive transport in III–V nanowire transistors. We find that at lower drain voltages the ballistic-to-diffusive crossover occurs at channel lengths of approximately 2.3 nm at room temperature. However, when we increase the drain voltage, we find that the ballistic-to-diffusive crossover can be more than nine times as long at room temperature. As the temperature is decreased, we find that the initially the performance is not significantly improved. However, as the temperature approaches 100 K, the ballistic-to-diffusive crossover increases to longer channel lengths quite dramatically. When InAs, InSb, and InP nanowires are compared at room temperature, we find that InAs and InSb perform in a similar fashion each with ballistic regions in excess of 10 nm, but that InP has no significant ballistic regime. Finally, we simulate several 10-nm InAs trigate transistors and show that for dopants deeply buried in the source and drain the devices appear ballistic, but when dopants appear near the source-channel interface, significant reductions in performance occur.**

***Index Terms*—Nanowire transistors (NWTs), phonon interactions, quantum simulation, III–V.**

I. Introduction

THE NANOWIRE transistor (NWT) [1] may be a viable device to replace bulk Si MOSFETs due to its ability to reduce short-channel effects and give greater control over the channel electron density. There has also been a resurgence in the exploration of III–V materials for next generation CMOS technology. While silicon is the unquestioned material of choice in CMOS technology, III–V materials have some advantages over silicon such as higher mobility, which could potentially lead to very high-speed low-power transistors. Of course, we recognize the tradeoff in terms of low density-of-states, i.e., Landauer channels. InSb has measured electron mobilities of 7.8×10^4 cm^2 V^{-1} $\cdot$ s^{-1} [2] and has long been touted as a good candidate for high-frequency devices. Recently, high-mobility wrap-gated p-channel InAs NWTs have been experimentally demonstrated which also have exceptionally high mobilities and solid device performance [3]. With the advent of technology capable of producing high quality III–V nanowires for transistor applications, it is natural to question the limits of device performance in III–V materials.

Manuscript received July 12, 2006; revised December 22, 2006. This work was supported by the SRC-NRI SWAN program. The review of this paper was arranged by Editor M. Reed.

The authors are with the Microelectronics Engineering Research Center, University of Texas at Austin, Austin, TX 78759 USA (e-mail: mgilbert@mer.utexas.edu; banerjee@ece.utexas.edu).

Color versions of one or more of the figures in this paper are available online at http://ieeexplore.ieee.org.

Digital Object Identifier 10.1109/TED.2007.891850

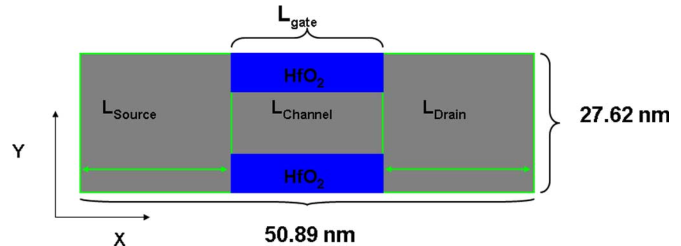

Fig. 1. Schematic of the device used in this paper taken in the xy plane.

Of particular interest for future generation CMOS applications is the location of the ballistic-to-diffusive crossover in III–V nanowire systems.

There have been many previous studies demonstrating the performance of silicon NWT [4]–[6] and InAs NWT [7]. However, since we are interested in operating these devices at or near room temperature, phonon processes are very important. A recent study has placed the ballistic-to-diffusive crossover for silicon nanowire systems at 1.42 nm [8]. This places serious limits on the effectiveness of silicon in next generation CMOS, but it also shows the importance of phonon modes in the determination of the performance characteristics. In this paper, we examine the dependence of the ballistic-to-diffusive (mobility dominated transport) crossover point in III–V NWT as a function of temperature, drain voltage, and semiconductor material covering three of the most popular III–V materials: InAs, InSb, and InP using a fully 3-D self-consistent quantum transport formalism. The effects of phonon scattering are included in the simulations as separable self-energy terms in the Hamiltonian. To make the simulations as complete as possible, we include interactions with the dopant ions, and inelastic effects (the effects of acoustic deformation potential, intervalley phonons [$\Gamma \rightarrow X$ and $\Gamma \rightarrow L$), and polar optical phonons (POPs)].

II. Device Structure and Simulation Method

In Fig. 1, we display a schematic of the system under consideration in the x–y plane (the z-axis is normal to the plane shown). The device dimensions (in multiples of the lattice constant) use in the simulations were chosen to aid in the inclusion of the discrete dopants. The thickness of the InAs layer is 9.09 nm and the width of the channel is 8.48 nm. The source and drain of the device are n-type with a doping density of 1.3×10^{18} cm^{-3}, while the channel of the device is considered to be p-type, but undoped. The gate material is assumed to be platinum and the gate oxide on each side is 1 nm of hafnium oxide (HfO_2). Underneath the device, we

0018-9383/$25.00 © 2007 IEEE

have assumed a thick silicon dioxide substrate. The length of the device is set to 50.89 nm. While the channel of the device is typically much smaller than the overall length of the device geometry, a large domain is set so that as the length of the channel is increased, the bandstructure for the overall device remains constant. The length of the channel starts at a length of 6.0583 Å and is increased by this length until the diffusive regime is obtained. During this increase of the length, the width, and depth of the nanowire channel are kept constant. The length of the gate that surrounds the nanowire on three sides is set to be the same length as the channel of the device. The source and drain of the device are divided equally depending on the length of the channel; however, they never are reduced below 10 nm in the x-direction.

Once the device geometry is defined, the InAs lattice is scanned and the dopants are distributed according to the method presented in [9]. Following the distribution of the dopants, they are then mapped back onto the grid of the simulation mesh and the initial self-consistent Poisson solution is obtained. In this case, the full Coulomb potential of the dopants is incorporated. Then, the solution of Poisson's equation for the local potential is no longer smoothly varying in the source and drain of the device. The inclusion of discrete dopants causes the formation of potential variations in the source and drain. The density throughout the device is calculated using a variant of the recursive scattering matrix method which solves the Schrödinger equation in the effective mass approximation, as described in [4]. In short, this method provides us with a 3-D, fully quantum mechanical treatment. Since the transport calculation is performed in real space, the different excited modes in the system are automatically coupled unlike in other simulations [6]. In order to achieve self-consistency, the density obtained from the transport calculation is then updated using Broyden's method [10] and a new guess for the potential is obtained through the solution of Poisson's equation. The process is repeated until a desired level of convergence is obtained. Exchange and correlations terms are included in each simulation through a local density approximation [11].

In this paper, we seek the ballistic-to-diffusive crossover in these nanowire systems. Our procedure for determining this quantity is given below. We know that even when the transport is ballistic, the lower limit of the resistance of the channel is determined by the inverse of the Landauer conductance

$$R_{\text{ballistic}} = \left[\frac{2e^2}{h}N\right]^{-1} \tag{1}$$

where N is the number of transverse modes flowing in the quantum wire. Clearly, the resistance in (1) has no dependence on the length of the quantum wire. Conversely, when the transport is determined by the carrier mobility and the carrier density, then the resistance becomes

$$R_{\text{diffusive}} = \frac{1}{ne\mu}\frac{L}{A} \tag{2}$$

where L is the channel length and A is the cross-sectional area of the inversion layer. We have been careful to use the area of the inversion layer rather than the width because we are dealing with a 3-D quantum wire with quantization in the transverse directions. In this regime, there is a clear linear dependence of the resistance with the length of the quantum wire channel.

III. POP Scattering

The inclusion of separable scattering mechanisms is not a new concept. In previous work, acoustic and optical phonon processes have been derived [8] and so the work will not be repeated here. However, we are now interested in including the nonlocal effects of POPs which, to this point, have not been treated. This is a crucial difference between silicon and III–V materials. In silicon, the local phonon processes dominate, but in III–V materials nonlocal optical processes dominate the room temperature transport. We begin by noting that to use the method presented in [8], we are assuming that the scattering is weak relative to the energies in the system, and that we are only interested in the steady-state limit. Therefore, we can use the Fermi golden rule expression, equivalent to a first-order nonself-consistent Born approximation, for each of the scattering processes and generate a real space self-energy from it. In particular, we note that the imaginary part of the self-energy term is related to the scattering rate and it is the latter scattering rate that we wish to calculate [8]. This will result in an x-directed momentum which is related to the carrier energy in the quantum wire. While the local scattering rates have been previously derived [8], we will present the important changes in the general derivation approach to take into account the nonlocal nature of POP scattering. In this paper, we use the Fermi golden rule to calculate scattering rates. This is treated in many other places, however, we must account for the transverse modes of the quantum wire. Therefore, we begin with the general form

$$\begin{aligned}\left(\frac{1}{\tau_{\text{polar}}}\right)_{ij}^{i'j'} &= \frac{\pi e^2}{\gamma V\omega_0}\sum_{q_x}\sum_{q_y,q_z}\int dy\int dz\int dy'\int dz' \\ &\quad\times \varphi_{i,j}^*(y,z)\varphi_{i',j'}(y,z)\varphi_{i,j}^*(y',z')\varphi_{i',j'}(y',z') \\ &\quad\times \frac{e^{iq_y(y-y')+iq_z(z-z')}}{q^2} \\ &\quad\times \{(N_q+1)\delta(E_k-E_{k-q}-\hbar\omega_0) \\ &\qquad + N_q\delta(E_k-E_{k-q}+\hbar\omega_0)\}\end{aligned} \tag{3}$$

where V is the volume, ω_0 is the phonon frequency and γ is the effective interaction parameter, i is the initial mode index in the width direction, j is the initial mode index in the depth direction, i' is the final mode index in the width direction, and j' is the final mode index in depth direction. The delta functions in (3) serve to conserve the energy in the process of the interactions of the carriers with the POPs. $\varphi_{i,j}(y,z)$ is the transverse 2-D wave function in the particular slice under consideration. We assume in this treatment that we are dealing with parabolic bandstructure. Taking a closer look at the terms

contained within the delta functions, we realize that based on this assumption

$$\begin{aligned} &E_k - E_{k\pm q} \pm \hbar\omega_0 \\ &\quad = E_{i,j} - E_{i',j'} \pm \hbar\omega_0 + \frac{\hbar^2 k_x^2}{2m_x^*} - \frac{\hbar^2 (k_x \pm q_x)^2}{2m_x^*} \\ &\quad = E_{i,j} - E_{i',j'} \pm \hbar\omega_0 - \frac{\hbar^2 k_x q_x}{m_x^*} \pm \frac{\hbar^2 q_x^2}{2m_x^2}. \end{aligned} \tag{4}$$

In (4), $E_{i,j}$ and $E_{i',j'}$ are the initial and final energies at the bottom of their respective bands. We begin to simplify (3), by first examining the longitudinal terms

$$\sum_{q_x} \frac{1}{2q^2} \delta(E_k - E_{k\pm q} \pm \hbar\omega_0). \tag{5}$$

We now expand (5) using the results from (4)

$$\sum_{q_x} \frac{1}{q_x^2 + q_y^2 + q_z^2} \delta\left(\mp \frac{\hbar^2 q_x^2}{2m_x^*} \mp \frac{\hbar^2 k_x q_x}{m_x^*} + E_{i,j} - E_{i',j'} \pm \hbar\omega_0\right). \tag{6}$$

This sum may be simplified further by taking the Fourier transform with respect to q_x

$$\frac{1}{2\pi} \int_{-\infty}^{\infty} \frac{dq_x e^{iq_x(x-x')}}{q_x^2 + q_y^2 + q_z^2} \delta\left(\mp \frac{\hbar^2 q_x^2}{2m_x^*} \mp \frac{\hbar^2 k_x q_x}{m_x^*} + \Delta_{i,j}^{i',j'}\right) \tag{7}$$

where we denote

$$\Delta_{i,j}^{i',j'} = E_{i,j} - E_{i',j'} \pm \hbar\omega_0. \tag{8}$$

Representing (7) as a summation, we have

$$\begin{aligned} &\frac{1}{2\pi} \int_{-\infty}^{\infty} \frac{dq_x e^{iq_x(x-x')}}{q_x^2 + q_y^2 + q_z^2} \frac{1}{|\partial E_{k\pm q}/\partial q_x|} \\ &\frac{m_x^*}{2\pi\hbar^2} \int_{-\infty}^{\infty} \frac{dq_x e^{iq_x(x-x')}}{q_x^2 + q_y^2 + q_z^2} \frac{1}{\left|\mp k_x + \frac{q_x}{2}\right|}. \end{aligned} \tag{9}$$

At this point, we examine the relationship for $E_{k\pm q}$

$$E_{k\pm q} = \frac{\hbar^2 k_x^2}{2m_x^*} \pm \frac{\hbar^2 k_x q_x}{m_x^*} + \frac{\hbar^2 q_x^2}{2m_x^*}. \tag{10}$$

Equation (10) is quadratic in q_x and may then be solved to yield a solution for q_x which is then substituted back into (9) making the term in the absolute value independent of q_x as shown below regardless of if the phonon process under consideration is emission or absorption. Therefore, we may group all of the variables that are independent of q_x into a simple dummy variable a. With this pairing, we may reduce our summation in (9) to reach

$$\frac{m_x^*}{2\pi\hbar^2} \int_{-\infty}^{\infty} \frac{dq_x e^{iq_x(x-x')}}{q_x^2 + a^2}. \tag{11}$$

Equation (11) is most easily evaluated by making a transformation to cylindrical coordinates to obtain

$$\frac{m_x^*}{4\pi\hbar^2} \iint \frac{q_x e^{iq_x\left(\overrightarrow{r} - \overrightarrow{r'}\right)}}{q_{xi}^2 + a^2} d\theta dq. \tag{12}$$

We evaluate the integral in (12) using contour integrations to arrive at a final, simplified expression for the sum over the longitudinal wavevectors

$$\sum_{q_x} \frac{1}{2q_x} \delta(E_k). \tag{13}$$

The expression in (13) is substituted back into (3) to find an overlap integral that is similar to both the one found in [8] and in most textbooks

$$\begin{aligned} &= \sum_{q_x} \sum_{q_y, q_z} \int dy \int dz \int dy' \int dz' \varphi_{i,j}^*(y,z) \varphi_{i',j'}(y,z) \\ &\quad \times \varphi_{i,j}^*(y',z') \varphi_{i',j'}(y',z') \frac{e^{iq_y(y-y')} + iq_z(z-z')}{2q_x} \delta(E_k) \\ &= \frac{A}{2V} \sum_{q_x} \iint dz dy \left[\varphi_{i,j}^*(y,z) \varphi_{i',j'}(y,z)\right]^2 \frac{1}{q_x} \delta(E_k) \\ &= \sum_{k_x} I_{i,j}^{i',j'} \frac{1}{k_x} \delta(E_k). \end{aligned} \tag{14}$$

Where in (14), we have used the following definition

$$I_{i,j}^{i',j'} = \frac{A}{4\pi V} \iint dy dz \left[\varphi_{i,j}^*(y,z) \varphi_{i',j'}(y,z)\right]^2. \tag{15}$$

Following the usual procedure, we replace the summation over the final momentum states with an integration

$$\sum_{k'} \to \frac{L}{2\pi} \int_{-\infty}^{\infty} dk' = \int_0^{\infty} \rho_{1D}(E') dE' \tag{16}$$

to obtain the final result

$$\left(\frac{1}{\tau_{\text{polar}}}\right)_{i,j}^{i',j'} = \frac{m_x^* L e^2}{32\pi^3 \gamma\omega_0} I_{i,j}^{i',j'} \int \frac{dk_x}{k_x} \delta(E_k). \tag{17}$$

However, we are still in the mode space representation and the longitudinal momentum is not yet a viable operator. From many-body physics, the momentum dependence arises from the Fourier transform of the differences in the two coordinates in the self-energy. Therefore, to include the proper momentum dependence, we take the inverse transform. This essentially involves solving a contour integral for both the emission and absorption cases which results from (17). This gives us our final, simplified and summarized results for absorption and emission of POPs

$$\left(\frac{1}{\tau_{\text{polar}}}\right)_{i,j}^{i',j'} = \frac{m_x^* L e^2}{32\pi^3 \gamma\omega_0} I_{i,j}^{i',j'} \begin{cases} N_q e^{-k_0|x-x'|} \\ (N_q+1) \frac{\sin(k_0|x-x'|)}{k_0|x-x'|} \end{cases}. \tag{18}$$

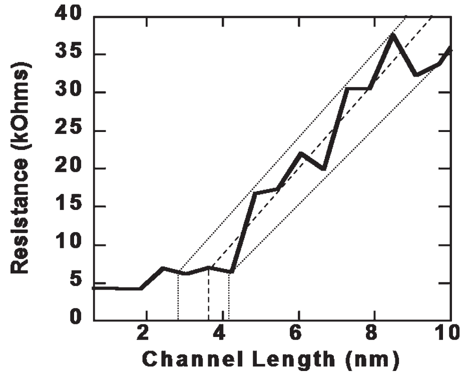

Fig. 2. Resistance of an InAs quantum wire as a function of the length of the channel. The gate voltage has been set to $V_g = 0.5$ V and the drain voltage has been set to $V_d = 10$ mV. The temperature of the device is 300 K. The red lines signify the maximum and minimum ranges for the ballistic to diffusive crossover, and the blue line signifies the median value. These lines are used to determine the value quoted for the ballistic to diffusive crossover.

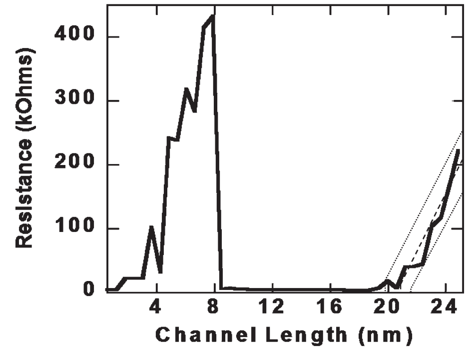

Fig. 3. Resistance of an InAs gated quantum wire as a function of the length of the channel. The gate voltage has been set to $V_g = 0.5$ V and the drain voltage has been set to $V_d = 0.5$ V. The temperature of the device is 300 K. The red lines once again signify the maximum and minimum ranges for the ballistic to diffusive crossover, and the blue line signifies the median value.

213 This result is reasonable as we now see the manifestation of 214 the nonlocal nature of POP scattering as a clear dependence on 215 distance in (18). To utilize this in the transport calculation, we 216 must use the following unitary transformation to convert this 217 form to the site representation for inclusion in the Hamiltonian

$$\Gamma_{\text{polar}} = \text{Im}\{\Sigma\} = U^{+} \left(\frac{\hbar}{\tau_{\text{polar}}} \right)_{i,j}^{i',j'} U \tag{19}$$

218 where U is a unitary mode-to-site transformation matrix. The 219 unitary matrix U^{+} results from the eigenvalue solutions in the 220 transverse slice and are composed of the various eigenfunc- 221 tions in the site basis. Hence, it represents a mode-to-slice 222 transformation.

223 IV. RESULTS

224 A. Drain-Voltage Dependence

225 In Fig. 2, we plot the resistance of an InAs quantum wire 226 as a function of the length of the channel for a small drain 227 bias of $V_d = 10$ mV. In each of the following plots, the gate 228 voltage is held constant at $V_g = 0.5$ V in order to ensure that 229 there is a channel in the p-type wire. It should be noted that the 230 optical phonon energy used in the calculation of InAs devices 231 is 30 meV. While the channel length remains below 3.6 nm, the 232 resistance of the device does not appear to change significantly. 233 The oscillations in the resistance in Fig. 2 arise mainly from 234 the interaction of the incident electron modes with the material 235 boundaries, and in particular, with the source and channel 236 interfaces creating strong quantum interference which is seen 237 not only in theoretical studies [12], [13] but also experimentally 238 [14]. For channels longer than about 3.6 nm, the resistance 239 shows a clear linear dependence as the channel length increases 240 as is expected when the nature of the transport changes from 241 ballistic to diffusive. At this drain voltage, we estimate the 242 ballistic-to-diffusive crossover to occur at 3.12 ± 0.3 nm. This 243 is limited by the strength of the POP scattering as the X and 244 L valleys are offset by sufficient energy to significantly limit the intervalley scattering rates to these valleys. While this value 245 is more than that of the quoted value of 1.42 nm for similar 246 cross-sectional silicon quantum wires, this is not the significant 247 increase we were hoping to see. Further, there will not be 248 significant device-to-device variation in InAs or other III–V 249 NWTs due to low concentration of dopant atoms as compared 250 to that of a typical silicon device. 251

In Fig. 3, we now increase the drain voltage to $V_d = 0.5$ V. 252 We find that this drain voltage consists of much more structure 253 than the device held at reduced drain voltages. We begin our 254 examination of Fig. 3, by noticing that there is an initial period 255 of slightly more than 3 nm where the resistance of the quantum 256 wire channel does not change. In this region, the length of the 257 channel is such that the incident electrons see almost no channel 258 potential and simply tunnel from the source to the drain of 259 the device. As the length of the channel is increased beyond 260 4 nm, we see that there is a large spike in the resistance of the 261 channel. This behavior is attributed to the fact that the locations 262 of the longitudinal states in the channel are too high in energy 263 to support any modes and the channel becomes a large tunnel 264 barrier. This argument is supported by the fact that the form of 265 the drain voltage versus channel length in the regime of 4 to 266 8 nm has an exponential form which is indicative of tunneling 267 transport. We do not see this in the lower drain voltage sweeps 268 due to the fact that scattering has blurred energy spectrum of 269 the electrons before they reach the channel. This widening of 270 the range of energies allows electrons not energetically capable 271 of accessing the states to scatter into them. Thus, we see no rise 272 in resistance in Fig. 2. While this type of interaction is fairly 273 uncommon in semiconductor devices due to their relatively 274 large sizes, this is common in systems of quasi-1-D electrons 275 connected to external reservoirs [13]. 276

The existence of the tunneling regime in Fig. 3 is an im- 277 portant point. If indeed, the physics is as we state then the 278 same tunneling regime should show up in simple ballistic 279 simulations of the same device structure. In Fig. 4, we plot 280 the resistance of the quantum wire channel as a function of its 281 length with no scattering included in the simulation. We find a 282 similar trend as in the case with the inelastic processes included. 283 In this simulation, we initially begin with three propagating 284 modes in the system. The initial resistances do not match the 285

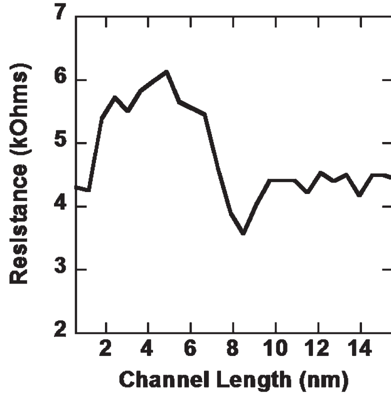

Fig. 4. Plot of the resistance of the quantum wire as a function of its length with no scattering included in the simulation for $V_g = V_d = 0.5$ V. We find the same short channel resistance trend in the ballistic case as we find in the case with the phonon processes included. Since the resistance increase in the quantum wires is the focus, we plot only the first 8 nm of channel length.

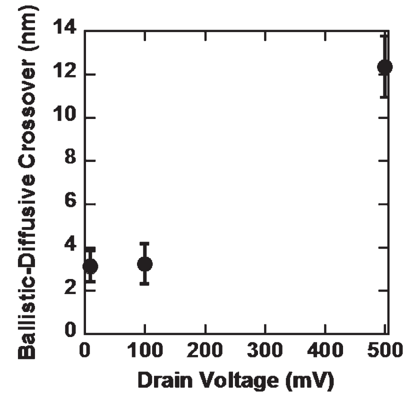

Fig. 5. Summary of the ballistic-to-diffusive crossover in InAs NWTs for different drain voltages at a constant gate voltage of $V_g = 0.5$ V. We see a nonlinear increasing trend forming in the ballistic-to-diffusive crossover length. This is due to the localization of POP scattering events.

other quantum wires as doping is slightly lower than in other devices. After a short period of nearly constant and quantized resistance, we see a similar rise in the resistance of the quantum wire as in the case where phonon interactions were included. Since no phonon modes are available to promote or demote the electron energies, we conclude that the tunneling regime is due to large energetic spacing of longitudinal states in the channel.

Therefore, while there is an initial ballistic region at high drain voltages, it is interrupted by a tunneling regime. After the tunneling regime, we see a dramatic reduction to the proper ballistic quantum resistance for several propagating modes. This ballistic region then persists, in the case of this specific device, for 12.33 ± 1.41 nm, after subtracting off the length of the tunneling region, before it begins to increase linearly as expected. This is almost 10 times the length found in a similar silicon NWT at room temperature.

In Fig. 5, we plot the ballistic-to-diffusive crossover as a function of the drain voltage applied to the device. There is an interesting trend present in this figure. We find that the ballistic-to-diffusive crossover seems to show a nonlinear increase with increasing drain voltage. This is quite different from the linearly reducing dependence on drain voltage found in silicon. To explain how this is possible, we reexamine the forms of the POP emission and absorption terms shown in (18). For low-energy carriers, the scattering rate is appreciable over a range of grid points in the longitudinal direction. This leads to large scattering rates which significantly affects the incident carriers. However, as the energy of the carriers is increased, the phonon scattering rates become local. This localization causes a significant reduction in the strength of the electron–phonon interaction contribution to the Hamiltonian. Therefore, we expect to see small ballistic-to-diffusive lengths at low drain energy **but** which increase as the carriers gain energy from the applied field. Perhaps the more unexpected part of this result is not that we obtain longer ballistic-to-diffusive lengths, but that the connection between the quasi-1-D electrons in the channel and the reservoirs produces a shift in the location of the ballistic regime. This is an important feature to note for future ultrasmall device fabrication as it imposes serious limits on the scalability of NWTs.

Put in more physical terms, we should expect to find the ballistic length to roughly follow

$$L_{\text{ballistic}} = \frac{eVt^2}{2mL}. \tag{20}$$

Where in (20), V is the applied voltage, t is the mean scattering time, L is the length of the channel, and m is the effective mass. Hence, by increasing the drain bias from 10 to 500 mV, we should find a corresponding increase of the ballistic length of 50 times. The fact that we do not see such a large increase is due to the fact that the mean scattering time is reduced significantly by hot carriers for the higher drain bias. This results in the value of about 12 nm for the ballistic length which is only an increase of 3.3 times compared to that of the low-voltage result. The reduction in the expected ballistic length corresponds to a decrease in the mean scattering time from 18 fs to about 8.5 fs. While these times are very short, this is indicative of the fact that the transport is not being conducted in a bulk sample. Using the bulk value of the mobility of InAs, we find that the mean scattering time is around 180 fs (assuming a mobility of $14\,000\ \text{cm}^2/\text{V}\cdot\text{s}$). If the carriers reach the saturation velocity, and drop the entire bias energy into longitudinal optical (LO) phonons, then the estimated mean scattering time would only be about 3.6 fs. Thus, the carriers are dropping a great deal of energy in the drain rather than in the channel of the device and our scattering time estimates seem to be in order.

B. Temperature Dependence

In Fig. 6, we once again plot the resistance of an InAs quantum wire device as a function of the channel length. As expected, as the device is cooled, the interactions with the phonon modes in the device should be reduced. We see that the initial 12 nm of the device exhibits the same type of behavior as in the higher temperature cases, however, now the tunneling regime now takes on a more pronounced appearance. This is due to the fact that there is no longer enough energy to broaden the levels in the channel and the energetic distribution of

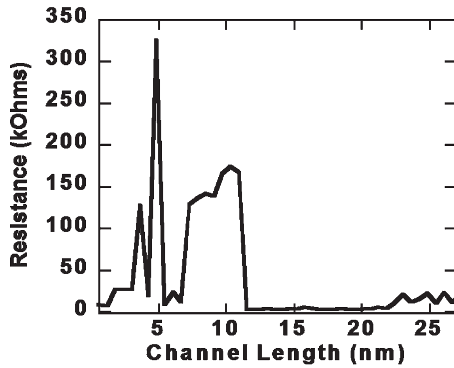

Fig. 6. Resistance of an InAs quantum wire as a function of the length of the channel. The gate voltage has been set to $V_g = 0.5$ V and the drain voltage has been set to $V_d = 0.5$ V. The temperature of the device is 100 K.

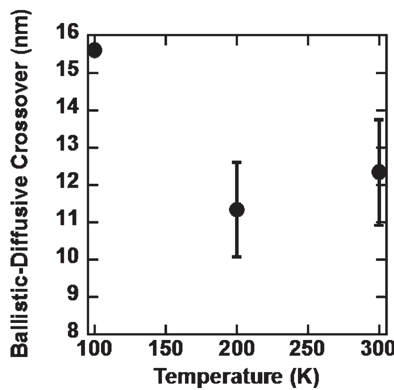

Fig. 7. Summary of the ballistic to diffusive crossover in InAs NWTs for temperatures at a constant voltages of $V_g = V_d = 0.5$ V. We see a decreasing nonlinear trend, within error bars, forming in the ballistic to diffusive crossover length. There are no error bars on the 100 K case as it is an estimate.

electrons becomes sharper. These effects cause the oscillations in conductance to become more pronounced. At temperatures this low, it is quite difficult to define a ballistic-to-diffusive length as the resistance never seems to begin to exhibit linear behavior. While the temperature is low, there is still enough thermal energy in the system so that the phonon modes are not completely frozen out, but here we find that the ballistic-to-diffusive crossover must occur at channel lengths in excess of 15.6 nm.

In Fig. 7, we summarize the performance of InAs NWT at several different temperatures. We find that the trend in the plot shows a quickly decaying dependence. Clearly, the mobility increases as the temperature is reduced. However, even at 100 K, POP scattering still dominates the transport. When this is coupled with the reduced size of the InAs NWT, we find that the scattering associated with POP phonons increases due to increased overlap integrals. Therefore, even at reduced temperatures the electron–phonon interactions are crucial to understanding the performance limits of III–V NWTs. It should be noted that these simulations do not account for the effect of carrier heating near the drain of the device. With a relatively large drain voltage of $V_d = 0.5$ V applied to the NWT, carrier heating will undoubted play a nontrivial role in determining the principles of thermal operation.

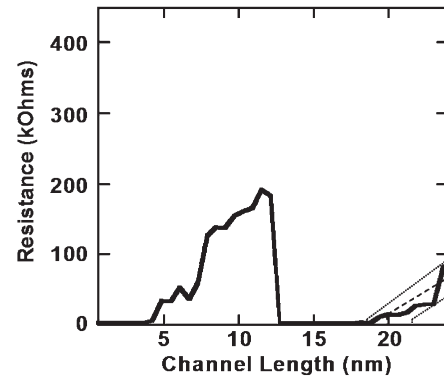

Fig. 8. Plot of the resistance of an InSb NWT as a function of the channel length with $V_g = V_d = 0.5$ V. We show the maximum and median lines used to estimate the ballistic to diffusive crossover.

C. Material Dependence

As mentioned in the introduction, InAs is not the only III–V semiconductor currently under investigation for future use in CMOS architectures; InSb and InP are also being considered. In Fig. 8, we plot the resistance of an InSb NWT as a function of channel length with the gate and drain voltages affixed at 0.5 V. The thickness of the InSb film is 9.07 nm and the width of the channel is 8.42 nm. The source and drain are n-type with doping set to 1.7×10^{18} cm^{-3} while the channel is undoped p-type. While the dimensions have again been chosen to facilitate the inclusion of the discrete doping in the source and the drain of the device, we have chosen very similar dimensions to the InAs devices to facilitate comparison. The overall width of the source and drain are 27.21 nm and the overall length of the device is 50.54 nm. In the InSb device, we see very similar trends as to those seen in the InAs devices. This is to be expected as their POP energies are quite similar. Nevertheless, while the overall shape of the curve remains similar, there are some notable differences. The location of the tunneling regime has shifted its position in channel length. This shift is attributed to the readjustment of the states in the channel due to the changes in effective mass between InAs and InSb. Therefore, the initial ballistic region associated with direct tunneling is estimated to be 4.73 ± 0.82 nm. After the tunneling region, we find a smooth ballistic region which extends 8.7 ± 0.60 nm, after subtracting off the tunneling region length. While the ballistic length in InSb and InAs NWTs are quite similar, the InAs device has a longer continuous region of ballistic transport. Based on these results, it seems that InAs and InSb are rather interchangeable.

Both InAs and InSb are starkly contrasted by the behavior of InP. In Fig. 9, we plot the resistance of an InP NWT as a function of the channel length for $V_g = V_d = 0.5$ V at 300 K. The dimensions of the device are slightly different due to the change in lattice constant. Here, we use a overall source and drain width of 27.58 nm with a total device length of 50.47 nm. The InP film thickness is 9.39 nm with a corresponding channel width of 8.22 nm. The channel is assumed to be undoped p-type and the source and drain are doped n-type 2×10^{18} cm^{-3}. In InP, we find that there is no significant ballistic transport regime and even very short NWTs show diffusive transport. This can

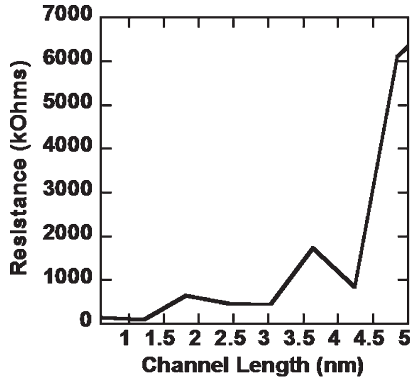

Fig. 9. Plot of the resistance of an InP NWT as a function of the channel length with $V_g = V_d = 0.5$ V. This material exhibits no ballistic regime under the conditions that we examined.

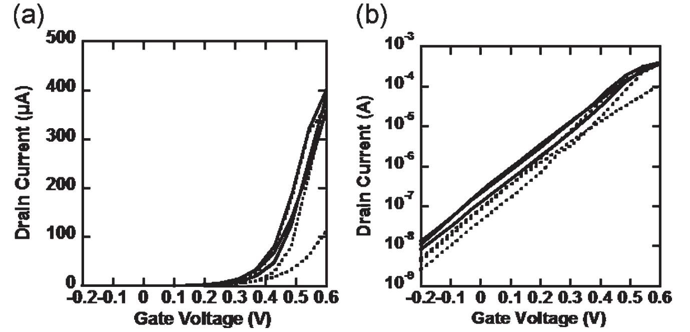

Fig. 10. (a) I_d–V_g curves for the elastic (solid) and a combination of elastic and inelastic (dotted) processes plotted on a linear scale. (b) I_d–V_g curves for the elastic (solid) and a combination of elastic and inelastic (dotted) processes plotted on a logarithmic scale.

425 be explained in two ways. First, the energy of the POPs in InP 426 is much larger than in InAs or InSb. When this is combined 427 with the larger effective mass of InP, the POP scattering rate 428 is quite large and ballistic transport cannot be obtained. More 429 importantly is the fact that InP demonstrates that the channel of 430 these NWT devices are strongly coupled to the source and the 431 drain. This affects transport in that the electrons are not injected 432 directly into the channel of the device. Before they reach the 433 channel, they must first traverse the source. Therefore, by the 434 time the electrons have reached the channel of the device, they 435 have already undergone diffusive transport and this has affected 436 the mean free path in InP. Almost certainly, it is possible for InP 437 to exhibit ballistic characteristics in other situations, but not in 438 the context of the device presented here.

439 *D. Effect of Discrete Doping*

440 In Fig. 10(a), we plot the I_d–V_g curve for three discretely 441 doped trigate InAs quantum wire devices with only elastic 442 (boundary and impurity) scattering considered (solid) and with 443 phonon processes (dotted) while in Fig. 10(b), we repeat the 444 plots again on a logarithmic scale. For device simulation, we 445 have increased the source and drain doping to 6×10^{18} cm^{-3} 446 and set the channel length to 9.69 nm. The device temperature 447 is 300 K and the drain voltage is held at $V_d = 0.6$ V. In terms 448 of simple device performance, averaging over four different 449 devices, we find that the threshold voltage is found to be 450 0.373 V $\pm$ 11 mV. These figures are slightly different from 451 those quoted elsewhere [9], but it should be noted that we have 452 used a smaller sampling of devices in this paper. While the 453 threshold voltage is, at present, too high for next generation 454 technology, with the use of gate stack engineering [7] this 455 figure can be brought down to acceptable levels. Further, we 456 see that the spread in the threshold voltage is quite small. This 457 is due to the fact that fewer dopant atoms are required to reach 458 these levels of performance. Thus, with fewer elastic scattering 459 sites to induce quantum interference, the threshold voltage is 460 expected to be more stable than in its silicon-based equivalents. 461 Upon further examination of the curves in Fig. 10(b), we find 462 that in the low gate voltage regime POP scattering significantly 463 reduces the current in all three cases. This shift in low gate 464 voltage current leads to modifications to the performance. The threshold voltage averaged over four devices is 0.423 V $\pm$ 465 7 mV. Based on this result, we find that the POP scattering 466 does indeed shift the threshold voltage, but it also reduces V_t 467 nonuniformities by reducing spread in carrier energy in the 468 source. At high gate voltages, we find that the drain currents 469 in both the elastic and combined (elastic scattering contribution 470 + inelastic scattering contribution) cases begin to merge after 471 $V_g = 0.5$ V. This can be most directly attributed to a high- 472 energy localization of the POP scattering rate which limits the 473 effect of the inelastic perturbations to current. The end result 474 is that the elastic interactions dominate the current–voltage 475 characteristics. 476

While in Fig. 10, the majority of the dopant atoms were 477 located near the bottom of the InAs layer allowing the de- 478 vice to recover quasi-ballistic behavior, one device shows a 479 very distinct difference between the ballistic and quasi-ballistic 480 cases. Here, the locations of the dopant atoms are such that in 481 the source of the device there are two dopant atoms near the 482 entrance to the channel in the middle of the semiconductor 483 layer. These dopant atoms cause significant modifications to 484 the energy of the incident electrons. The lower energy electrons 485 now see more POP scattering which, when combined with the 486 typical reflections from the channel entrance, gives rise to sig- 487 nificant reductions in the amount of charge in the channel. With 488 less conduction in the channel, the device sees significantly 489 degraded performance. 490

In Fig. 11, we plot the electron density taken at a depth of 491 approximately 5 nm into the InAs device layer at $V_g = 0.6$ V 492 for the elastic case. The black dots in the figure represent the 493 locations of the dopant atoms in the system. Dots that are 494 larger in size are closer to the surface of the device, while 495 dots that are smaller are buried farther down in the device. 496 At this voltage, we are above the threshold voltage for the 497 device; the channel is now heavily populated with carriers. 498 In the source and drain, the location of the electron density 499 depends rather weakly on the locations of the dopants. This 500 is mainly due to the scarcity of the dopants and that they are 501 buried deeply in the InAs substrate which reduces their effect 502 on the propagating electrons. Nevertheless, the density tends to 503 roughly follow the path of the dopants as it makes its way to the 504 channel. In the channel, we find that the some of the electrons 505 have been trapped by multiple sequential reflections off of the 506

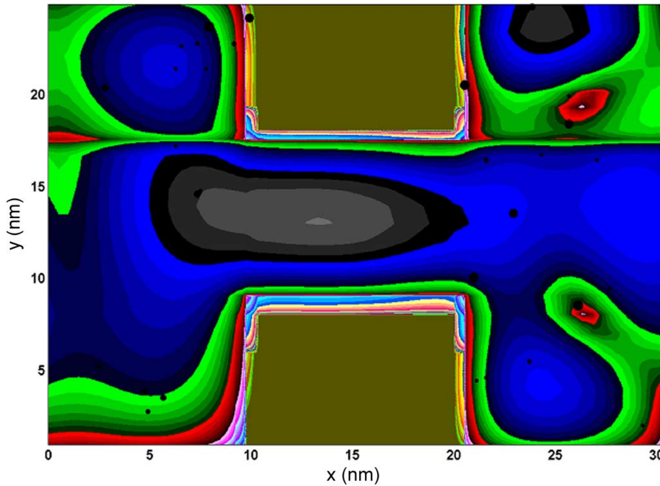

Fig. 11. Plot of the electron density in the xy plane taken at a depth of 5 nm into the InAs semiconductor layer at $V_g = V_d = 0.6$ V. The black dots represent the locations of the dopant atoms in the source and drain of the device. Larger dots represent atoms that are closer to the surface while smaller dots are more deeply buried in the semiconductor layer. At these biases, the channel is fully populated and the quantum interference is minimal.

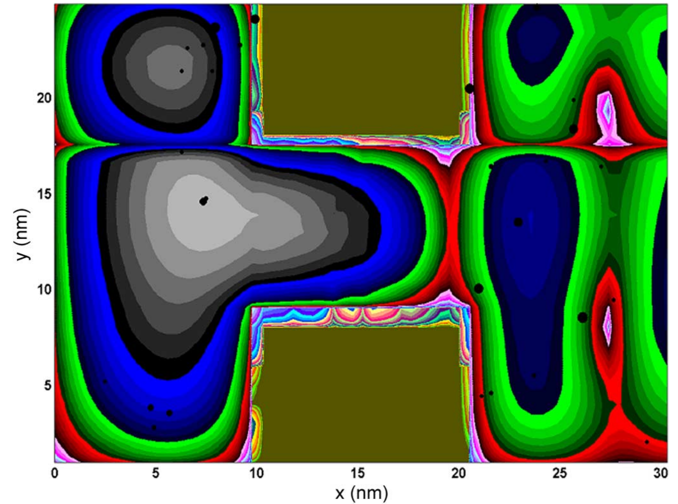

Fig. 12. Plot of the electron density in the xy plane taken at a depth of 5 nm into the InAs semiconductor layer at $V_g = V_d = 0.6$ V. The black dots represent the locations of the dopant atoms in the source and drain of the device. Here, there is significant charge build-up near the source-channel interface due to the combination of interference with the dopants near this interface and POPs.

source-channel and channel-drain interfaces. As the electrons then exit the channel, they begin to populate sites in the drain that are energetically preferential.

In Fig. 12, we plot the density at $V_g = 0.6$ V for the combined (elastic + inelastic) case. We see very distinct differences in the location and magnitude of the electrons in the combined case, but, in general, it follows the same general trend as in the elastic case. With the combined case, we find that there is a pronounced buildup of charge in the area of the source near the channel entrance of 0.38 k_bT. The reflection off of this interface alters the energy of the carriers to the point where some of the lower energy modes will see increased scattering and a reduction in density of approximately 0.25 k_bT in most areas. In the source, we find additional discrepancies as this is the location where the scattering is most prevalent. In the channel and drain of the device, we find that there is a corresponding reduction of electron density as much of the incident density has been reflected at the channel interface.

V. Conclusion

In this paper, we have presented a method for including the nonlocal effects of POP scattering into simulation techniques relying on a propagating Hamiltonian. We then used this method to simulate III–V NWTs while including the effects of not only POP scattering, but also impurity, intervalley, and acoustic phonon scattering. In InAs devices, we find that NWTs have a significant ballistic length at room temperature of about 12.33 nm. This ballistic length increases nonlinearly as the drain voltage increases as the nonlocal POPs become localized at higher energy. Further, we find that reductions in temperature will not improve the ballistic-to-diffusive crossover length, but cooling the device to around 100 K improves the performance greatly due to weak phonon interactions. InSb devices have similar device performance, with a ballistic-to-diffusive crossover of about 8.7 nm. The great difference between InAs and InSb is the locations of longitudinal states in the channel which shifts a highly resistive region responsible for poor device performance in both materials. This is not the case with InP where we find that the POP scattering is too strong and diffusive transport is achieved in the source of the device. We simulated several 10-nm InAs devices to find that at high gate voltages they behave as ballistic devices, but the placement of dopants in the source and drain is crucial to device performance. These results demonstrate the potential and limitations of III–V NWTs for use in highly scaled CMOS architectures. With ballistic lengths nine times longer than silicon, they are certainly worthy of continued exploration for novel electron quantum interference and waveguide devices.

Acknowledgment

M. J. Gilbert, one of the authors, would like to thank D. K Ferry and L. F. Register for insightful conversations.

References

[1] B. S. Doyle, S. Datta, M. Doczy, S. Hareland, B. Jin, J. Kavalieros, T. Linton, A. Murthy, R. Rios, and R. Chau, “High performance fully-depleted tri-gate CMOS transistors,” *IEEE Electron Device Lett.*, vol. 24, no. 4, pp. 463–465, Apr. 2003.

[2] T. Ashley, A. B. Dean, C. T. Elliott, G. J. Pryce, A. D. Johnson, and H. Willis, “Uncooled high-speed InSb field-effect transistors,” *Appl. Phys. Lett.*, vol. 66, no. 4, pp. 481–483, Jan. 1995.

[3] T. Bryllert, L.-E. Wernersson, L. E. Fröberg, and L. Samuelson, “Vertical high-mobility wrap-gated InAs nanowire transistor,” *IEEE Electron Device Lett.*, vol. 27, no. 5, pp. 323–325, May 2006.

[4] M. J. Gilbert and D. K. Ferry, “Efficient quantum three-dimensional modeling of fully-depleted ballistic silicon-on-insulator metal–oxide–semiconductor field-effect transistors,” *J. Appl. Phys.*, vol. 95, no. 12, pp. 7954–7960, Jun. 2004.

[5] ——, “Quantum interference in fully-depleted tri-gate quantum wire transistors—The role of inelastic scattering,” *IEEE Trans. Nanotechnol.*, vol. 4, no. 5, pp. 599–604, Sep. 2005.

[6] J. Wang, E. Polizzi, and M. Lundstrom, “A three-dimensional quantum simulation of silicon nanowire transistors with the effective-mass approximation,” *J. Appl. Phys.*, vol. 96, no. 4, pp. 2192–2203, Aug. 2004.

578 [7] M. J. Gilbert and D. K. Ferry, “Indium arsenide quantum wire trigate
579 metal oxide semiconductor field effect transistor,” *J. Appl. Phys.*, vol. 99,
580 no. 12, p. 054 503, 2006.
581 [8] M. J. Gilbert, R. Akis, and D. K. Ferry, “Phonon assisted ballistic to
582 diffusive crossover in silicon nanowire transistors,” *J. Appl. Phys.*, vol. 98,
583 no. 9, p. 094 303, Nov. 2005.
584 [9] M. J. Gilbert and D. K. Ferry, “Discrete dopant effects in ultra-small fully
585 depleted ballistic SOI MOSFETs,” *Superlattices Microstruct.*, vol. 34,
586 no. 3–6, pp. 277–282, Sep. 2003.
587 [10] D. D. Johnson, “Modified Broyden’s method for accelerating convergence
588 in self-consistent calculations,” *Phys. Rev. B, Condens. Matter*, vol. 38,
589 no. 18, pp. 12 807–12 813, Dec. 1988.
590 [11] Y. Wang, J. Wang, H. Guo, and E. Zaremba, “Many electron effects
591 on ballistic transport,” *Phys. Rev. B, Condens. Matter*, vol. 52, no. 4,
592 pp. 2738–2746, Jul. 1995.
593 [12] V. A. Sablikov, S. V. Polyakov, and M. Büttiker, “Charging effects in a
594 quantum wire with leads,” *Phys. Rev. B, Condens. Matter*, vol. 61, no. 20,
595 pp. 13 763–13 773, May 2000.
596 [13] G. Kirczenow, “Resonant conduction in ballistic quantum channels,”
597 *Phys. Rev. B, Condens. Matter*, vol. 39, no. 14, pp. 10 452–10 455,
598 May 1989.
599 [14] A. T. Tilke, F. C. Simmel, H. Lorenz, R. H. Blick, and J. P. Kotthaus,
600 “Quantum interference in a one-dimensional silicon nanowire,” *Phys. Rev.
601 B, Condens. Matter*, vol. 68, no. 7, p. 075 311, Aug. 2003.

602 **M. J. Gilbert** (M’06) received the B.S. (with hon-
603 ors), M.S., and Ph.D. degrees in electrical engineer-
604 ing, all from Arizona State University, Tempe, in
605 2000, 2003, and 2005, respectively.
606 He is the Assistant Director of the South West
607 Academy of Nanoelectronics at the University of
608 Texas at Austin. He has contributed to research
609 on quantum computing, decoherence mechanisms
610 in nanostructures, many-body theory, and quantum
611 transport. He has authored more than 30 refereed
612 publications and has given presentations at over
613 30 international conferences. His current research centers on spintronics,
614 strongly correlated electron systems, and quantum transport theory.

Sanjay K. Banerjee (S’80–M’83–SM’89–F’96) re- 615
ceived the B.Tech. degree from the Indian Institute 616
of Technology (IIT), Kharagpur, India, in 1979, and 617
the M.S. and Ph.D. degrees from the University of 618
Illinois at Urbana–Champaign, in 1981 and 1983, 619
respectively, all in electrical engineering. 620
He is the Cockrell Family Regents Chair Pro- 621
fessor of Electrical and Computer Engineering and 622
Director of the Microelectronics Research Center at 623
the University of Texas at Austin. As a Member of 624
Technical Staff, Corporate Research, Development 625
and Engineering of Texas Instruments, Inc., from 1983–1987, he worked 626
on polysilicon transistors and dynamic random access trench memory cells 627
used by Texas Instruments in the world’s first 4-Mb dynamic random access 628
memory. He has been Assistant Professor (1987–1990), Associate Professor 629
(1990–1993), and Professor (since 1993) with The University of Texas at 630
Austin. He is currently active in the areas of ultrahigh vacuum and remote 631
plasma-enhanced chemical vapor deposition for silicon–germanium–carbon 632
heterostructure MOSFETs and nanostructures. He is also interested in the areas 633
of ultrashallow junction technology and semiconductor device modeling. He 634
has over 580 archival refereed publications/talks, seven books/chapters, and 635
26 U.S. patents. He has supervised over 40 Ph.D. and 50 M.S. students. 636
Dr. Banerjee was corecipient of the Best Paper Award, IEEE International 637
Solid State Circuits Conference in 1986. He received the Engineering Founda- 638
tion Advisory Council Halliburton Award in 1991, the Texas Atomic Energy 639
Fellowship (1990–1997), Cullen Professorship (1997–2001), and the National 640
Science Foundation Presidential Young Investigator Award in 1988. His recent 641
awards include Fellow of APS (2006), Distinguished Alumnus Award, IIT 642
(2005), Industrial R&D 100 Award (with Singh in 2004), Electro-Chemical 643
Society (ECS) Callinan Award, 2003, IEEE Millennium Medal, 2000, and 644
Semiconductor Research Corporation Inventor Recognition Award, 2000. He 645
was a Distinguished Lecturer for IEEE Electron Devices Society and the 646
General Chair of the IEEE Device Research Conference, 2002. 647

Ballistic to Diffusive Crossover in III–V Nanowire Transistors

M. J. Gilbert, *Member, IEEE*, and Sanjay K. Banerjee, *Fellow, IEEE*

***Abstract*—In this paper, we examine the crossover between ballistic and diffusive transport in III–V nanowire transistors. We find that at lower drain voltages the ballistic-to-diffusive crossover occurs at channel lengths of approximately 2.3 nm at room temperature. However, when we increase the drain voltage, we find that the ballistic-to-diffusive crossover can be more than nine times as long at room temperature. As the temperature is decreased, we find that the initially the performance is not significantly improved. However, as the temperature approaches 100 K, the ballistic-to-diffusive crossover increases to longer channel lengths quite dramatically. When InAs, InSb, and InP nanowires are compared at room temperature, we find that InAs and InSb perform in a similar fashion each with ballistic regions in excess of 10 nm, but that InP has no significant ballistic regime. Finally, we simulate several 10-nm InAs trigate transistors and show that for dopants deeply buried in the source and drain the devices appear ballistic, but when dopants appear near the source-channel interface, significant reductions in performance occur.**

***Index Terms*—Nanowire transistors (NWTs), phonon interactions, quantum simulation, III–V.**

I. INTRODUCTION

THE NANOWIRE transistor (NWT) [1] may be a viable device to replace bulk Si MOSFETs due to its ability to reduce short-channel effects and give greater control over the channel electron density. There has also been a resurgence in the exploration of III–V materials for next generation CMOS technology. While silicon is the unquestioned material of choice in CMOS technology, III–V materials have some advantages over silicon such as higher mobility, which could potentially lead to very high-speed low-power transistors. Of course, we recognize the tradeoff in terms of low density-of-states, i.e., Landauer channels. InSb has measured electron mobilities of 7.8×10^4 cm^2 $\mathrm{V}^{-1} \cdot \mathrm{s}^{-1}$ [2] and has long been touted as a good candidate for high-frequency devices. Recently, high-mobility wrap-gated p-channel InAs NWTs have been experimentally demonstrated which also have exceptionally high mobilities and solid device performance [3]. With the advent of technology capable of producing high quality III–V nanowires for transistor applications, it is natural to question the limits of device performance in III–V materials.

Manuscript received July 12, 2006; revised December 22, 2006. This work was supported by the SRC-NRI SWAN program. The review of this paper was arranged by Editor M. Reed.

The authors are with the Microelectronics Engineering Research Center, University of Texas at Austin, Austin, TX 78759 USA (e-mail: mgilbert@mer.utexas.edu; banerjee@ece.utexas.edu).

Color versions of one or more of the figures in this paper are available online at http://ieeexplore.ieee.org.

Digital Object Identifier 10.1109/TED.2007.891850

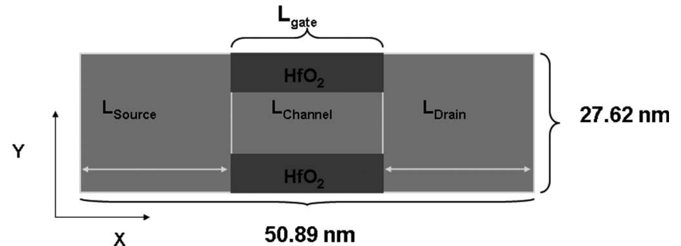

Fig. 1. Schematic of the device used in this paper taken in the xy plane.

Of particular interest for future generation CMOS applications is the location of the ballistic-to-diffusive crossover in III–V nanowire systems.

There have been many previous studies demonstrating the performance of silicon NWT [4]–[6] and InAs NWT [7]. However, since we are interested in operating these devices at or near room temperature, phonon processes are very important. A recent study has placed the ballistic-to-diffusive crossover for silicon nanowire systems at 1.42 nm [8]. This places serious limits on the effectiveness of silicon in next generation CMOS, but it also shows the importance of phonon modes in the determination of the performance characteristics. In this paper, we examine the dependence of the ballistic-to-diffusive (mobility dominated transport) crossover point in III–V NWT as a function of temperature, drain voltage, and semiconductor material covering three of the most popular III–V materials: InAs, InSb, and InP using a fully 3-D self-consistent quantum transport formalism. The effects of phonon scattering are included in the simulations as separable self-energy terms in the Hamiltonian. To make the simulations as complete as possible, we include interactions with the dopant ions, and inelastic effects (the effects of acoustic deformation potential, intervalley phonons [$\Gamma \rightarrow X$ and $\Gamma \rightarrow L$), and polar optical phonons (POPs)].

II. DEVICE STRUCTURE AND SIMULATION METHOD

In Fig. 1, we display a schematic of the system under consideration in the x–y plane (the z-axis is normal to the plane shown). The device dimensions (in multiples of the lattice constant) use in the simulations were chosen to aid in the inclusion of the discrete dopants. The thickness of the InAs layer is 9.09 nm and the width of the channel is 8.48 nm. The source and drain of the device are n-type with a doping density of 1.3×10^{18} cm^{-3}, while the channel of the device is considered to be p-type, but undoped. The gate material is assumed to be platinum and the gate oxide on each side is 1 nm of hafnium oxide (HfO_2). Underneath the device, we

0018-9383/$25.00 © 2007 IEEE

have assumed a thick silicon dioxide substrate. The length of the device is set to 50.89 nm. While the channel of the device is typically much smaller than the overall length of the device geometry, a large domain is set so that as the length of the channel is increased, the bandstructure for the overall device remains constant. The length of the channel starts at a length of 6.0583 Å and is increased by this length until the diffusive regime is obtained. During this increase of the length, the width, and depth of the nanowire channel are kept constant. The length of the gate that surrounds the nanowire on three sides is set to be the same length as the channel of the device. The source and drain of the device are divided equally depending on the length of the channel; however, they never are reduced below 10 nm in the x-direction.

Once the device geometry is defined, the InAs lattice is scanned and the dopants are distributed according to the method presented in [9]. Following the distribution of the dopants, they are then mapped back onto the grid of the simulation mesh and the initial self-consistent Poisson solution is obtained. In this case, the full Coulomb potential of the dopants is incorporated. Then, the solution of Poisson's equation for the local potential is no longer smoothly varying in the source and drain of the device. The inclusion of discrete dopants causes the formation of potential variations in the source and drain. The density throughout the device is calculated using a variant of the recursive scattering matrix method which solves the Schrödinger equation in the effective mass approximation, as described in [4]. In short, this method provides us with a 3-D, fully quantum mechanical treatment. Since the transport calculation is performed in real space, the different excited modes in the system are automatically coupled unlike in other simulations [6]. In order to achieve self-consistency, the density obtained from the transport calculation is then updated using Broyden's method [10] and a new guess for the potential is obtained through the solution of Poisson's equation. The process is repeated until a desired level of convergence is obtained. Exchange and correlations terms are included in each simulation through a local density approximation [11].

In this paper, we seek the ballistic-to-diffusive crossover in these nanowire systems. Our procedure for determining this quantity is given below. We know that even when the transport is ballistic, the lower limit of the resistance of the channel is determined by the inverse of the Landauer conductance

$$R_{\text{ballistic}} = \left[\frac{2e^2}{h}N\right]^{-1} \tag{1}$$

where N is the number of transverse modes flowing in the quantum wire. Clearly, the resistance in (1) has no dependence on the length of the quantum wire. Conversely, when the transport is determined by the carrier mobility and the carrier density, then the resistance becomes

$$R_{\text{diffusive}} = \frac{1}{ne\mu}\frac{L}{A} \tag{2}$$

where L is the channel length and A is the cross-sectional area of the inversion layer. We have been careful to use the area of the inversion layer rather than the width because we are dealing with a 3-D quantum wire with quantization in the transverse directions. In this regime, there is a clear linear dependence of the resistance with the length of the quantum wire channel.

III. POP Scattering

The inclusion of separable scattering mechanisms is not a new concept. In previous work, acoustic and optical phonon processes have been derived [8] and so the work will not be repeated here. However, we are now interested in including the nonlocal effects of POPs which, to this point, have not been treated. This is a crucial difference between silicon and III–V materials. In silicon, the local phonon processes dominate, but in III–V materials nonlocal optical processes dominate the room temperature transport. We begin by noting that to use the method presented in [8], we are assuming that the scattering is weak relative to the energies in the system, and that we are only interested in the steady-state limit. Therefore, we can use the Fermi golden rule expression, equivalent to a first-order nonself-consistent Born approximation, for each of the scattering processes and generate a real space self-energy from it. In particular, we note that the imaginary part of the self-energy term is related to the scattering rate and it is the latter scattering rate that we wish to calculate [8]. This will result in an x-directed momentum which is related to the carrier energy in the quantum wire. While the local scattering rates have been previously derived [8], we will present the important changes in the general derivation approach to take into account the nonlocal nature of POP scattering. In this paper, we use the Fermi golden rule to calculate scattering rates. This is treated in many other places, however, we must account for the transverse modes of the quantum wire. Therefore, we begin with the general form

$$\begin{aligned}\left(\frac{1}{\tau_{\text{polar}}}\right)_{ij}^{i'j'} &= \frac{\pi e^2}{\gamma V \omega_0}\sum_{q_x}\sum_{q_y,q_z}\int dy\int dz\int dy'\int dz' \\ &\quad\times \varphi_{i,j}^*(y,z)\varphi_{i',j'}(y,z)\varphi_{i,j}^*(y',z')\varphi_{i',j'}(y',z') \\ &\quad\times \frac{e^{iq_y(y-y')+iq_z(z-z')}}{q^2} \\ &\quad\times \{(N_q+1)\delta(E_k-E_{k-q}-\hbar\omega_0) \\ &\qquad + N_q\delta(E_k-E_{k-q}+\hbar\omega_0)\}\end{aligned} \tag{3}$$

where V is the volume, ω_0 is the phonon frequency and γ is the effective interaction parameter, i is the initial mode index in the width direction, j is the initial mode index in the depth direction, i' is the final mode index in the width direction, and j' is the final mode index in depth direction. The delta functions in (3) serve to conserve the energy in the process of the interactions of the carriers with the POPs. $\varphi_{i,j}(y,z)$ is the transverse 2-D wave function in the particular slice under consideration. We assume in this treatment that we are dealing with parabolic bandstructure. Taking a closer look at the terms

172 contained within the delta functions, we realize that based on
173 this assumption

$$\begin{aligned} E_k - E_{k\pm q} \pm \hbar\omega_0 &= E_{i,j} - E_{i',j'} \pm \hbar\omega_0 + \frac{\hbar^2 k_x^2}{2m_x^*} - \frac{\hbar^2(k_x \pm q_x)^2}{2m_x^*} \\ &= E_{i,j} - E_{i',j'} \pm \hbar\omega_0 - \frac{\hbar^2 k_x q_x}{m_x^*} \pm \frac{\hbar^2 q_x^2}{2m_x^2}. \end{aligned} \tag{4}$$

174 In (4), $E_{i,j}$ and $E_{i',j'}$ are the initial and final energies at the
175 bottom of their respective bands. We begin to simplify (3), by
176 first examining the longitudinal terms

$$\sum_{q_x} \frac{1}{2q^2} \delta(E_k - E_{k\pm q} \pm \hbar\omega_0). \tag{5}$$

177 We now expand (5) using the results from (4)

$$\sum_{q_x} \frac{1}{q_x^2+q_y^2+q_z^2} \delta\left(\mp\frac{\hbar^2 q_x^2}{2m_x^*} \mp \frac{\hbar^2 k_x q_x}{m_x^*} + E_{i,j} - E_{i',j'} \pm \hbar\omega_0\right). \tag{6}$$

178 This sum may be simplified further by taking the Fourier
179 transform with respect to q_x

$$\frac{1}{2\pi} \int_{-\infty}^{\infty} \frac{dq_x e^{iq_x(x-x')}}{q_x^2+q_y^2+q_z^2} \delta\left(\mp\frac{\hbar^2 q_x^2}{2m_x^*} \mp \frac{\hbar^2 k_x q_x}{m_x^*} + \Delta_{i,j}^{i',j'}\right) \tag{7}$$

180 where we denote

$$\Delta_{i,j}^{i',j'} = E_{i,j} - E_{i',j'} \pm \hbar\omega_0. \tag{8}$$

181 Representing (7) as a summation, we have

$$\begin{aligned} &\frac{1}{2\pi} \int_{-\infty}^{\infty} \frac{dq_x e^{iq_x(x-x')}}{q_x^2+q_y^2+q_z^2} \frac{1}{|\partial E_{k\pm q}/\partial q_x|} \\ &\frac{m_x^*}{2\pi\hbar^2} \int_{-\infty}^{\infty} \frac{dq_x e^{iq_x(x-x')}}{q_x^2+q_y^2+q_z^2} \frac{1}{\left|\mp k_x + \frac{q_x}{2}\right|}. \end{aligned} \tag{9}$$

182 At this point, we examine the relationship for $E_{k\pm q}$

$$E_{k\pm q} = \frac{\hbar^2 k_x^2}{2m_x^*} \pm \frac{\hbar^2 k_x q_x}{m_x^*} + \frac{\hbar^2 q_x^2}{2m_x^*}. \tag{10}$$

183 Equation (10) is quadratic in q_x and may then be solved to yield
184 a solution for q_x which is then substituted back into (9) making
185 the term in the absolute value independent of q_x as shown
186 below regardless of if the phonon process under consideration
187 is emission or absorption. Therefore, we may group all of
188 the variables that are independent of q_x into a simple dummy
189 variable a. With this pairing, we may reduce our summation in
190 (9) to reach

$$\frac{m_x^*}{2\pi\hbar^2} \int_{-\infty}^{\infty} \frac{dq_x e^{iq_x(x-x')}}{q_x^2+a^2}. \tag{11}$$

Equation (11) is most easily evaluated by making a transforma- 191
tion to cylindrical coordinates to obtain 192

$$\frac{m_x^*}{4\pi\hbar^2} \iint \frac{q_x e^{iq_x\left(\overrightarrow{r} - \overrightarrow{r'}\right)}}{q_{xi}^2 + a^2} d\theta dq. \tag{12}$$

We evaluate the integral in (12) using contour integrations to 193
arrive at a final, simplified expression for the sum over the 194
longitudinal wavevectors 195

$$\sum_{q_x} \frac{1}{2q_x} \delta(E_k). \tag{13}$$

The expression in (13) is substituted back into (3) to find an 196
overlap integral that is similar to both the one found in [8] and 197
in most textbooks 198

$$\begin{aligned} &= \sum_{q_x} \sum_{q_y,q_z} \int dy \int dz \int dy' \int dz' \varphi_{i,j}^*(y,z) \varphi_{i',j'}(y,z) \\ &\times \varphi_{i,j}^*(y',z') \varphi_{i',j'}(y',z') \frac{e^{iq_y(y-y')} + iq_z(z-z')}{2q_x} \delta(E_k) \\ &= \frac{A}{2V} \sum_{q_x} \iint dz dy \left[\varphi_{i,j}^*(y,z) \varphi_{i',j'}(y,z)\right]^2 \frac{1}{q_x} \delta(E_k) \\ &= \sum_{k_x} I_{i,j}^{i',j'} \frac{1}{k_x} \delta(E_k). \end{aligned} \tag{14}$$

Where in (14), we have used the following definition 199

$$I_{i,j}^{i',j'} = \frac{A}{4\pi V} \iint dy dz \left[\varphi_{i,j}^*(y,z) \varphi_{i',j'}(y,z)\right]^2. \tag{15}$$

Following the usual procedure, we replace the summation over 200
the final momentum states with an integration 201

$$\sum_{k'} \to \frac{L}{2\pi} \int_{-\infty}^{\infty} dk' = \int_{0}^{\infty} \rho_{1D}(E') dE' \tag{16}$$

to obtain the final result 202

$$\left(\frac{1}{\tau_{\text{polar}}}\right)_{i,j}^{i',j'} = \frac{m_x^* L e^2}{32\pi^3 \gamma\omega_0} I_{i,j}^{i',j'} \int \frac{dk_x}{k_x} \delta(E_k). \tag{17}$$

However, we are still in the mode space representation and 203
the longitudinal momentum is not yet a viable operator. From 204
many-body physics, the momentum dependence arises from the 205
Fourier transform of the differences in the two coordinates in 206
the self-energy. Therefore, to include the proper momentum 207
dependence, we take the inverse transform. This essentially 208
involves solving a contour integral for both the emission and 209
absorption cases which results from (17). This gives us our 210
final, simplified and summarized results for absorption and 211
emission of POPs 212

$$\left(\frac{1}{\tau_{\text{polar}}}\right)_{i,j}^{i',j'} = \frac{m_x^* L e^2}{32\pi^3 \gamma\omega_0} I_{i,j}^{i',j'} \begin{cases} N_q e^{-k_0|x-x'|} \\ (N_q+1) \frac{\sin(k_0|x-x'|)}{k_0|x-x'|} \end{cases}. \tag{18}$$

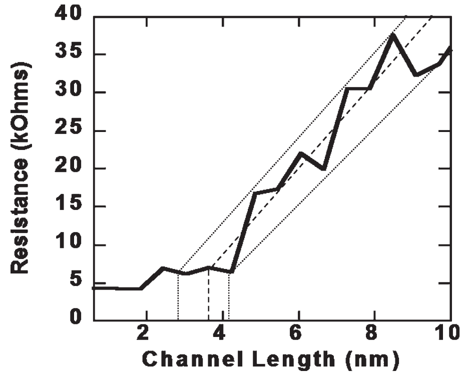

Fig. 2. Resistance of an InAs quantum wire as a function of the length of the channel. The gate voltage has been set to $V_g = 0.5$ V and the drain voltage has been set to $V_d = 10$ mV. The temperature of the device is 300 K. The red lines signify the maximum and minimum ranges for the ballistic to diffusive crossover, and the blue line signifies the median value. These lines are used to determine the value quoted for the ballistic to diffusive crossover.

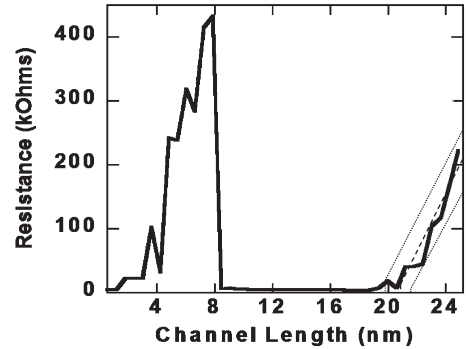

Fig. 3. Resistance of an InAs gated quantum wire as a function of the length of the channel. The gate voltage has been set to $V_g = 0.5$ V and the drain voltage has been set to $V_d = 0.5$ V. The temperature of the device is 300 K. The red lines once again signify the maximum and minimum ranges for the ballistic to diffusive crossover, and the blue line signifies the median value.

This result is reasonable as we now see the manifestation of the nonlocal nature of POP scattering as a clear dependence on distance in (18). To utilize this in the transport calculation, we must use the following unitary transformation to convert this form to the site representation for inclusion in the Hamiltonian

$$\Gamma_{\text{polar}} = \text{Im}\{\Sigma\} = U^{+} \left(\frac{\hbar}{\tau_{\text{polar}}} \right)_{i,j}^{i',j'} U \tag{19}$$

where U is a unitary mode-to-site transformation matrix. The unitary matrix U^{+} results from the eigenvalue solutions in the transverse slice and are composed of the various eigenfunctions in the site basis. Hence, it represents a mode-to-slice transformation.

IV. Results

A. Drain-Voltage Dependence

In Fig. 2, we plot the resistance of an InAs quantum wire as a function of the length of the channel for a small drain bias of $V_d = 10$ mV. In each of the following plots, the gate voltage is held constant at $V_g = 0.5$ V in order to ensure that there is a channel in the p-type wire. It should be noted that the optical phonon energy used in the calculation of InAs devices is 30 meV. While the channel length remains below 3.6 nm, the resistance of the device does not appear to change significantly. The oscillations in the resistance in Fig. 2 arise mainly from the interaction of the incident electron modes with the material boundaries, and in particular, with the source and channel interfaces creating strong quantum interference which is seen not only in theoretical studies [12], [13] but also experimentally [14]. For channels longer than about 3.6 nm, the resistance shows a clear linear dependence as the channel length increases as is expected when the nature of the transport changes from ballistic to diffusive. At this drain voltage, we estimate the ballistic-to-diffusive crossover to occur at 3.12 ± 0.3 nm. This is limited by the strength of the POP scattering as the X and L valleys are offset by sufficient energy to significantly limit the intervalley scattering rates to these valleys. While this value is more than that of the quoted value of 1.42 nm for similar cross-sectional silicon quantum wires, this is not the significant increase we were hoping to see. Further, there will not be significant device-to-device variation in InAs or other III–V NWTs due to low concentration of dopant atoms as compared to that of a typical silicon device.

In Fig. 3, we now increase the drain voltage to $V_d = 0.5$ V. We find that this drain voltage consists of much more structure than the device held at reduced drain voltages. We begin our examination of Fig. 3, by noticing that there is an initial period of slightly more than 3 nm where the resistance of the quantum wire channel does not change. In this region, the length of the channel is such that the incident electrons see almost no channel potential and simply tunnel from the source to the drain of the device. As the length of the channel is increased beyond 4 nm, we see that there is a large spike in the resistance of the channel. This behavior is attributed to the fact that the locations of the longitudinal states in the channel are too high in energy to support any modes and the channel becomes a large tunnel barrier. This argument is supported by the fact that the form of the drain voltage versus channel length in the regime of 4 to 8 nm has an exponential form which is indicative of tunneling transport. We do not see this in the lower drain voltage sweeps due to the fact that scattering has blurred energy spectrum of the electrons before they reach the channel. This widening of the range of energies allows electrons not energetically capable of accessing the states to scatter into them. Thus, we see no rise in resistance in Fig. 2. While this type of interaction is fairly uncommon in semiconductor devices due to their relatively large sizes, this is common in systems of quasi-1-D electrons connected to external reservoirs [13].

The existence of the tunneling regime in Fig. 3 is an important point. If indeed, the physics is as we state then the same tunneling regime should show up in simple ballistic simulations of the same device structure. In Fig. 4, we plot the resistance of the quantum wire channel as a function of its length with no scattering included in the simulation. We find a similar trend as in the case with the inelastic processes included. In this simulation, we initially begin with three propagating modes in the system. The initial resistances do not match the

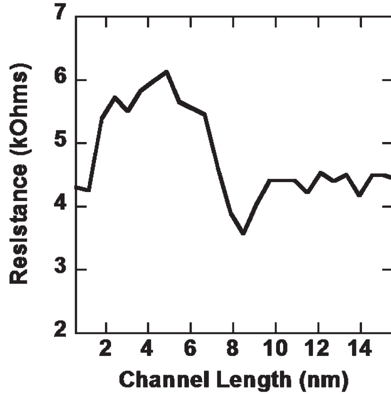

Fig. 4. Plot of the resistance of the quantum wire as a function of its length with no scattering included in the simulation for $V_g = V_d = 0.5$ V. We find the same short channel resistance trend in the ballistic case as we find in the case with the phonon processes included. Since the resistance increase in the quantum wires is the focus, we plot only the first 8 nm of channel length.

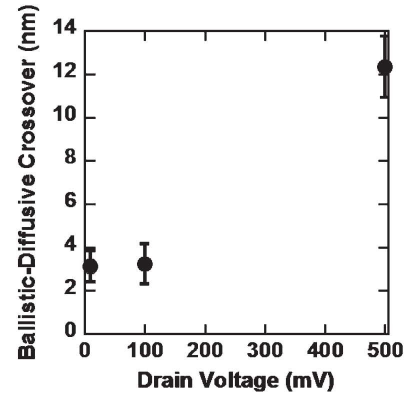

Fig. 5. Summary of the ballistic-to-diffusive crossover in InAs NWTs for different drain voltages at a constant gate voltage of $V_g = 0.5$ V. We see a nonlinear increasing trend forming in the ballistic-to-diffusive crossover length. This is due to the localization of POP scattering events.

286 other quantum wires as doping is slightly lower than in other 287 devices. After a short period of nearly constant and quantized 288 resistance, we see a similar rise in the resistance of the quantum 289 wire as in the case where phonon interactions were included. 290 Since no phonon modes are available to promote or demote 291 the electron energies, we conclude that the tunneling regime 292 is due to large energetic spacing of longitudinal states in 293 the channel.

294 Therefore, while there is an initial ballistic region at high 295 drain voltages, it is interrupted by a tunneling regime. After 296 the tunneling regime, we see a dramatic reduction to the proper 297 ballistic quantum resistance for several propagating modes. 298 This ballistic region then persists, in the case of this specific 299 device, for 12.33 ± 1.41 nm, after subtracting off the length 300 of the tunneling region, before it begins to increase linearly as 301 expected. This is almost 10 times the length found in a similar 302 silicon NWT at room temperature.

303 In Fig. 5, we plot the ballistic-to-diffusive crossover as a 304 function of the drain voltage applied to the device. There 305 is an interesting trend present in this figure. We find that 306 the ballistic-to-diffusive crossover seems to show a nonlinear 307 increase with increasing drain voltage. This is quite different 308 from the linearly reducing dependence on drain voltage found 309 in silicon. To explain how this is possible, we reexamine the 310 forms of the POP emission and absorption terms shown in (18). 311 For low-energy carriers, the scattering rate is appreciable over 312 a range of grid points in the longitudinal direction. This leads 313 to large scattering rates which significantly affects the incident 314 carriers. However, as the energy of the carriers is increased, the 315 phonon scattering rates become local. This localization causes 316 a significant reduction in the strength of the electron–phonon 317 interaction contribution to the Hamiltonian. Therefore, we ex- 318 pect to see small ballistic-to-diffusive lengths at low drain 319 energy **but** which increase as the carriers gain energy from the 320 applied field. Perhaps the more unexpected part of this result is 321 not that we obtain longer ballistic-to-diffusive lengths, but that 322 the connection between the quasi-1-D electrons in the channel 323 and the reservoirs produces a shift in the location of the ballistic 324 regime. This is an important feature to note for future ultrasmall device fabrication as it imposes serious limits on the scalability 325 of NWTs. 326

Put in more physical terms, we should expect to find the 327 ballistic length to roughly follow 328

$$L_{\text{ballistic}} = \frac{eVt^2}{2mL}. \quad (20)$$

Where in (20), V is the applied voltage, t is the mean scattering 329 time, L is the length of the channel, and m is the effective mass. 330 Hence, by increasing the drain bias from 10 to 500 mV, we 331 should find a corresponding increase of the ballistic length of 332 50 times. The fact that we do not see such a large increase is due 333 to the fact that the mean scattering time is reduced significantly 334 by hot carriers for the higher drain bias. This results in the 335 value of about 12 nm for the ballistic length which is only an 336 increase of 3.3 times compared to that of the low-voltage result. 337 The reduction in the expected ballistic length corresponds to 338 a decrease in the mean scattering time from 18 fs to about 339 8.5 fs. While these times are very short, this is indicative of the 340 fact that the transport is not being conducted in a bulk sample. 341 Using the bulk value of the mobility of InAs, we find that the 342 mean scattering time is around 180 fs (assuming a mobility of 343 $14\,000\ \text{cm}^2/\text{V} \cdot \text{s}$). If the carriers reach the saturation velocity, 344 and drop the entire bias energy into longitudinal optical (LO) 345 phonons, then the estimated mean scattering time would only 346 be about 3.6 fs. Thus, the carriers are dropping a great deal of 347 energy in the drain rather than in the channel of the device and 348 our scattering time estimates seem to be in order. 349

B. Temperature Dependence 350

In Fig. 6, we once again plot the resistance of an InAs 351 quantum wire device as a function of the channel length. As 352 expected, as the device is cooled, the interactions with the 353 phonon modes in the device should be reduced. We see that the 354 initial 12 nm of the device exhibits the same type of behavior 355 as in the higher temperature cases, however, now the tunneling 356 regime now takes on a more pronounced appearance. This is 357 due to the fact that there is no longer enough energy to broaden 358 the levels in the channel and the energetic distribution of 359

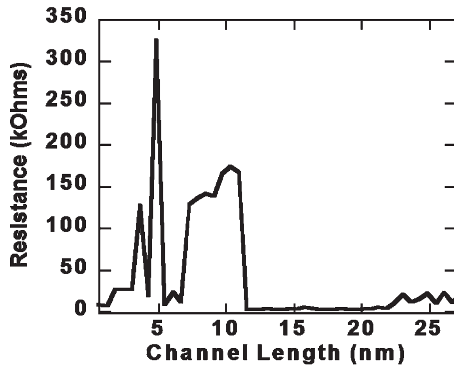

Fig. 6. Resistance of an InAs quantum wire as a function of the length of the channel. The gate voltage has been set to $V_g = 0.5$ V and the drain voltage has been set to $V_d = 0.5$ V. The temperature of the device is 100 K.

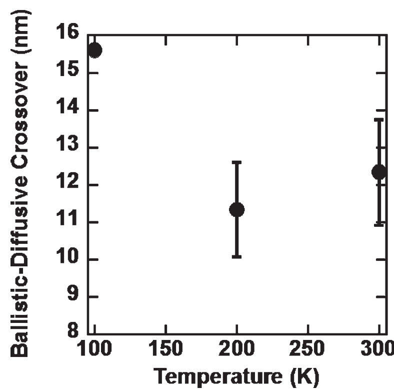

Fig. 7. Summary of the ballistic to diffusive crossover in InAs NWTs for temperatures at a constant voltages of $V_g = V_d = 0.5$ V. We see a decreasing nonlinear trend, within error bars, forming in the ballistic to diffusive crossover length. There are no error bars on the 100 K case as it is an estimate.

electrons becomes sharper. These effects cause the oscillations in conductance to become more pronounced. At temperatures this low, it is quite difficult to define a ballistic-to-diffusive length as the resistance never seems to begin to exhibit linear behavior. While the temperature is low, there is still enough thermal energy in the system so that the phonon modes are not completely frozen out, but here we find that the ballistic-to-diffusive crossover must occur at channel lengths in excess of 15.6 nm.

In Fig. 7, we summarize the performance of InAs NWT at several different temperatures. We find that the trend in the plot shows a quickly decaying dependence. Clearly, the mobility increases as the temperature is reduced. However, even at 100 K, POP scattering still dominates the transport. When this is coupled with the reduced size of the InAs NWT, we find that the scattering associated with POP phonons increases due to increased overlap integrals. Therefore, even at reduced temperatures the electron–phonon interactions are crucial to understanding the performance limits of III–V NWTs. It should be noted that these simulations do not account for the effect of carrier heating near the drain of the device. With a relatively large drain voltage of $V_d = 0.5$ V applied to the NWT, carrier heating will undoubted play a nontrivial role in determining the principles of thermal operation.

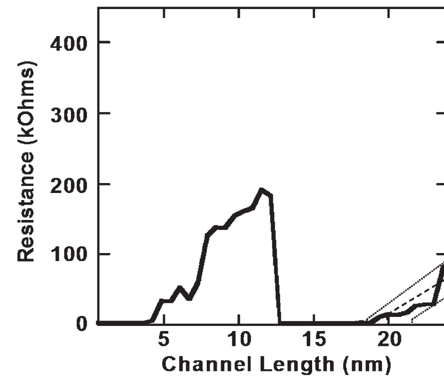

Fig. 8. Plot of the resistance of an InSb NWT as a function of the channel length with $V_g = V_d = 0.5$ V. We show the maximum and median lines used to estimate the ballistic to diffusive crossover.

C. Material Dependence

As mentioned in the introduction, InAs is not the only III–V semiconductor currently under investigation for future use in CMOS architectures; InSb and InP are also being considered. In Fig. 8, we plot the resistance of an InSb NWT as a function of channel length with the gate and drain voltages affixed at 0.5 V. The thickness of the InSb film is 9.07 nm and the width of the channel is 8.42 nm. The source and drain are n-type with doping set to 1.7×10^{18} cm^{-3} while the channel is undoped p-type. While the dimensions have again been chosen to facilitate the inclusion of the discrete doping in the source and the drain of the device, we have chosen very similar dimensions to the InAs devices to facilitate comparison. The overall width of the source and drain are 27.21 nm and the overall length of the device is 50.54 nm. In the InSb device, we see very similar trends as to those seen in the InAs devices. This is to be expected as their POP energies are quite similar. Nevertheless, while the overall shape of the curve remains similar, there are some notable differences. The location of the tunneling regime has shifted its position in channel length. This shift is attributed to the readjustment of the states in the channel due to the changes in effective mass between InAs and InSb. Therefore, the initial ballistic region associated with direct tunneling is estimated to be 4.73 ± 0.82 nm. After the tunneling region, we find a smooth ballistic region which extends 8.7 ± 0.60 nm, after subtracting off the tunneling region length. While the ballistic length in InSb and InAs NWTs are quite similar, the InAs device has a longer continuous region of ballistic transport. Based on these results, it seems that InAs and InSb are rather interchangeable.

Both InAs and InSb are starkly contrasted by the behavior of InP. In Fig. 9, we plot the resistance of an InP NWT as a function of the channel length for $V_g = V_d = 0.5$ V at 300 K. The dimensions of the device are slightly different due to the change in lattice constant. Here, we use a overall source and drain width of 27.58 nm with a total device length of 50.47 nm. The InP film thickness is 9.39 nm with a corresponding channel width of 8.22 nm. The channel is assumed to be undoped p-type and the source and drain are doped n-type 2×10^{18} cm^{-3}. In InP, we find that there is no significant ballistic transport regime and even very short NWTs show diffusive transport. This can

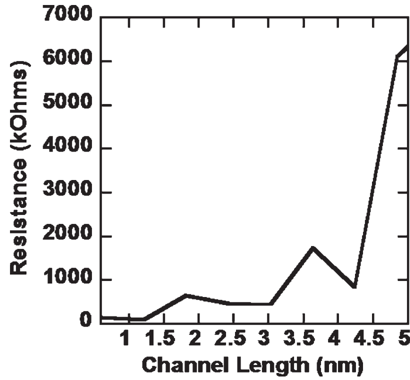

Fig. 9. Plot of the resistance of an InP NWT as a function of the channel length with $V_g = V_d = 0.5$ V. This material exhibits no ballistic regime under the conditions that we examined.

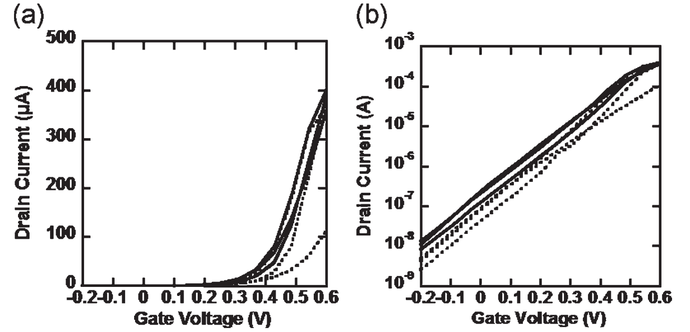

Fig. 10. (a) I_d–V_g curves for the elastic (solid) and a combination of elastic and inelastic (dotted) processes plotted on a linear scale. (b) I_d–V_g curves for the elastic (solid) and a combination of elastic and inelastic (dotted) processes plotted on a logarithmic scale.

425 be explained in two ways. First, the energy of the POPs in InP 426 is much larger than in InAs or InSb. When this is combined 427 with the larger effective mass of InP, the POP scattering rate 428 is quite large and ballistic transport cannot be obtained. More 429 importantly is the fact that InP demonstrates that the channel of 430 these NWT devices are strongly coupled to the source and the 431 drain. This affects transport in that the electrons are not injected 432 directly into the channel of the device. Before they reach the 433 channel, they must first traverse the source. Therefore, by the 434 time the electrons have reached the channel of the device, they 435 have already undergone diffusive transport and this has affected 436 the mean free path in InP. Almost certainly, it is possible for InP 437 to exhibit ballistic characteristics in other situations, but not in 438 the context of the device presented here.

439 *D. Effect of Discrete Doping*

440 In Fig. 10(a), we plot the I_d–V_g curve for three discretely 441 doped trigate InAs quantum wire devices with only elastic 442 (boundary and impurity) scattering considered (solid) and with 443 phonon processes (dotted) while in Fig. 10(b), we repeat the 444 plots again on a logarithmic scale. For device simulation, we 445 have increased the source and drain doping to 6×10^{18} cm^{-3} 446 and set the channel length to 9.69 nm. The device temperature 447 is 300 K and the drain voltage is held at $V_d = 0.6$ V. In terms 448 of simple device performance, averaging over four different 449 devices, we find that the threshold voltage is found to be 450 0.373 V $\pm$ 11 mV. These figures are slightly different from 451 those quoted elsewhere [9], but it should be noted that we have 452 used a smaller sampling of devices in this paper. While the 453 threshold voltage is, at present, too high for next generation 454 technology, with the use of gate stack engineering [7] this 455 figure can be brought down to acceptable levels. Further, we 456 see that the spread in the threshold voltage is quite small. This 457 is due to the fact that fewer dopant atoms are required to reach 458 these levels of performance. Thus, with fewer elastic scattering 459 sites to induce quantum interference, the threshold voltage is 460 expected to be more stable than in its silicon-based equivalents. 461 Upon further examination of the curves in Fig. 10(b), we find 462 that in the low gate voltage regime POP scattering significantly 463 reduces the current in all three cases. This shift in low gate 464 voltage current leads to modifications to the performance. The threshold voltage averaged over four devices is 0.423 V $\pm$ 465 7 mV. Based on this result, we find that the POP scattering 466 does indeed shift the threshold voltage, but it also reduces V_t 467 nonuniformities by reducing spread in carrier energy in the 468 source. At high gate voltages, we find that the drain currents 469 in both the elastic and combined (elastic scattering contribution 470 + inelastic scattering contribution) cases begin to merge after 471 $V_g = 0.5$ V. This can be most directly attributed to a high- 472 energy localization of the POP scattering rate which limits the 473 effect of the inelastic perturbations to current. The end result 474 is that the elastic interactions dominate the current–voltage 475 characteristics. 476

While in Fig. 10, the majority of the dopant atoms were 477 located near the bottom of the InAs layer allowing the de- 478 vice to recover quasi-ballistic behavior, one device shows a 479 very distinct difference between the ballistic and quasi-ballistic 480 cases. Here, the locations of the dopant atoms are such that in 481 the source of the device there are two dopant atoms near the 482 entrance to the channel in the middle of the semiconductor 483 layer. These dopant atoms cause significant modifications to 484 the energy of the incident electrons. The lower energy electrons 485 now see more POP scattering which, when combined with the 486 typical reflections from the channel entrance, gives rise to sig- 487 nificant reductions in the amount of charge in the channel. With 488 less conduction in the channel, the device sees significantly 489 degraded performance. 490

In Fig. 11, we plot the electron density taken at a depth of 491 approximately 5 nm into the InAs device layer at $V_g = 0.6$ V 492 for the elastic case. The black dots in the figure represent the 493 locations of the dopant atoms in the system. Dots that are 494 larger in size are closer to the surface of the device, while 495 dots that are smaller are buried farther down in the device. 496 At this voltage, we are above the threshold voltage for the 497 device; the channel is now heavily populated with carriers. 498 In the source and drain, the location of the electron density 499 depends rather weakly on the locations of the dopants. This 500 is mainly due to the scarcity of the dopants and that they are 501 buried deeply in the InAs substrate which reduces their effect 502 on the propagating electrons. Nevertheless, the density tends to 503 roughly follow the path of the dopants as it makes its way to the 504 channel. In the channel, we find that the some of the electrons 505 have been trapped by multiple sequential reflections off of the 506

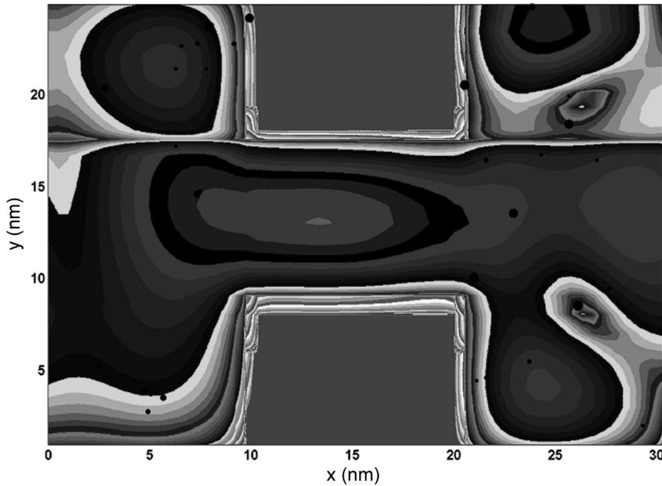

Fig. 11. Plot of the electron density in the xy plane taken at a depth of 5 nm into the InAs semiconductor layer at $V_g = V_d = 0.6$ V. The black dots represent the locations of the dopant atoms in the source and drain of the device. Larger dots represent atoms that are closer to the surface while smaller dots are more deeply buried in the semiconductor layer. At these biases, the channel is fully populated and the quantum interference is minimal.

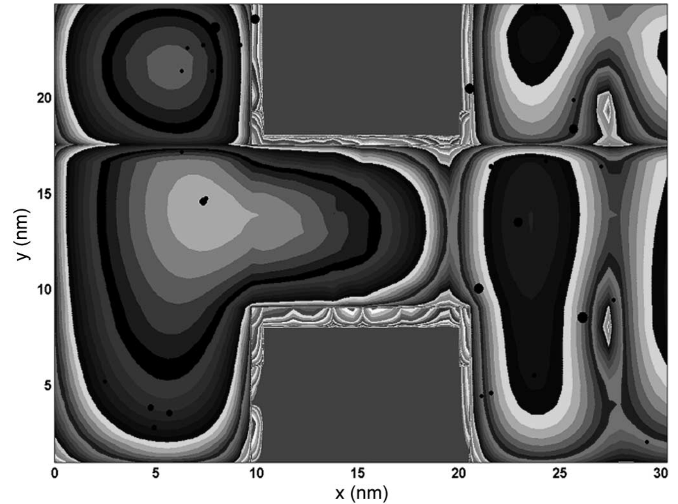

Fig. 12. Plot of the electron density in the xy plane taken at a depth of 5 nm into the InAs semiconductor layer at $V_g = V_d = 0.6$ V. The black dots represent the locations of the dopant atoms in the source and drain of the device. Here, there is significant charge build-up near the source-channel interface due to the combination of interference with the dopants near this interface and POPs.

source-channel and channel-drain interfaces. As the electrons then exit the channel, they begin to populate sites in the drain that are energetically preferential.

In Fig. 12, we plot the density at $V_g = 0.6$ V for the combined (elastic + inelastic) case. We see very distinct differences in the location and magnitude of the electrons in the combined case, but, in general, it follows the same general trend as in the elastic case. With the combined case, we find that there is a pronounced buildup of charge in the area of the source near the channel entrance of 0.38 k_bT. The reflection off of this interface alters the energy of the carriers to the point where some of the lower energy modes will see increased scattering and a reduction in density of approximately 0.25 k_bT in most areas. In the source, we find additional discrepancies as this is the location where the scattering is most prevalent. In the channel and drain of the device, we find that there is a corresponding reduction of electron density as much of the incident density has been reflected at the channel interface.

V. Conclusion

In this paper, we have presented a method for including the nonlocal effects of POP scattering into simulation techniques relying on a propagating Hamiltonian. We then used this method to simulate III–V NWTs while including the effects of not only POP scattering, but also impurity, intervalley, and acoustic phonon scattering. In InAs devices, we find that NWTs have a significant ballistic length at room temperature of about 12.33 nm. This ballistic length increases nonlinearly as the drain voltage increases as the nonlocal POPs become localized at higher energy. Further, we find that reductions in temperature will not improve the ballistic-to-diffusive crossover length, but cooling the device to around 100 K improves the performance greatly due to weak phonon interactions. InSb devices have similar device performance, with a ballistic-to-diffusive crossover of about 8.7 nm. The great difference between InAs and InSb is the locations of longitudinal states in the channel which shifts a highly resistive region responsible for poor device performance in both materials. This is not the case with InP where we find that the POP scattering is too strong and diffusive transport is achieved in the source of the device. We simulated several 10-nm InAs devices to find that at high gate voltages they behave as ballistic devices, but the placement of dopants in the source and drain is crucial to device performance. These results demonstrate the potential and limitations of III–V NWTs for use in highly scaled CMOS architectures. With ballistic lengths nine times longer than silicon, they are certainly worthy of continued exploration for novel electron quantum interference and waveguide devices.

Acknowledgment

M. J. Gilbert, one of the authors, would like to thank D. K Ferry and L. F. Register for insightful conversations.

References

[1] B. S. Doyle, S. Datta, M. Doczy, S. Hareland, B. Jin, J. Kavalieros, T. Linton, A. Murthy, R. Rios, and R. Chau, "High performance fully-depleted tri-gate CMOS transistors," *IEEE Electron Device Lett.*, vol. 24, no. 4, pp. 463–465, Apr. 2003.

[2] T. Ashley, A. B. Dean, C. T. Elliott, G. J. Pryce, A. D. Johnson, and H. Willis, "Uncooled high-speed InSb field-effect transistors," *Appl. Phys. Lett.*, vol. 66, no. 4, pp. 481–483, Jan. 1995.

[3] T. Bryllert, L.-E. Wernersson, L. E. Fröberg, and L. Samuelson, "Vertical high-mobility wrap-gated InAs nanowire transistor," *IEEE Electron Device Lett.*, vol. 27, no. 5, pp. 323–325, May 2006.

[4] M. J. Gilbert and D. K. Ferry, "Efficient quantum three-dimensional modeling of fully-depleted ballistic silicon-on-insulator metal–oxide–semiconductor field-effect transistors," *J. Appl. Phys.*, vol. 95, no. 12, pp. 7954–7960, Jun. 2004.

[5] ——, "Quantum interference in fully-depleted tri-gate quantum wire transistors—The role of inelastic scattering," *IEEE Trans. Nanotechnol.*, vol. 4, no. 5, pp. 599–604, Sep. 2005.

[6] J. Wang, E. Polizzi, and M. Lundstrom, "A three-dimensional quantum simulation of silicon nanowire transistors with the effective-mass approximation," *J. Appl. Phys.*, vol. 96, no. 4, pp. 2192–2203, Aug. 2004.

[7] M. J. Gilbert and D. K. Ferry, "Indium arsenide quantum wire trigate metal oxide semiconductor field effect transistor," *J. Appl. Phys.*, vol. 99, no. 12, p. 054 503, 2006.
[8] M. J. Gilbert, R. Akis, and D. K. Ferry, "Phonon assisted ballistic to diffusive crossover in silicon nanowire transistors," *J. Appl. Phys.*, vol. 98, no. 9, p. 094 303, Nov. 2005.
[9] M. J. Gilbert and D. K. Ferry, "Discrete dopant effects in ultra-small fully depleted ballistic SOI MOSFETs," *Superlattices Microstruct.*, vol. 34, no. 3–6, pp. 277–282, Sep. 2003.
[10] D. D. Johnson, "Modified Broyden's method for accelerating convergence in self-consistent calculations," *Phys. Rev. B, Condens. Matter*, vol. 38, no. 18, pp. 12 807–12 813, Dec. 1988.
[11] Y. Wang, J. Wang, H. Guo, and E. Zaremba, "Many electron effects on ballistic transport," *Phys. Rev. B, Condens. Matter*, vol. 52, no. 4, pp. 2738–2746, Jul. 1995.
[12] V. A. Sablikov, S. V. Polyakov, and M. Büttiker, "Charging effects in a quantum wire with leads," *Phys. Rev. B, Condens. Matter*, vol. 61, no. 20, pp. 13 763–13 773, May 2000.
[13] G. Kirczenow, "Resonant conduction in ballistic quantum channels," *Phys. Rev. B, Condens. Matter*, vol. 39, no. 14, pp. 10 452–10 455, May 1989.
[14] A. T. Tilke, F. C. Simmel, H. Lorenz, R. H. Blick, and J. P. Kotthaus, "Quantum interference in a one-dimensional silicon nanowire," *Phys. Rev. B, Condens. Matter*, vol. 68, no. 7, p. 075 311, Aug. 2003.

M. J. Gilbert (M'06) received the B.S. (with honors), M.S., and Ph.D. degrees in electrical engineering, all from Arizona State University, Tempe, in 2000, 2003, and 2005, respectively.

He is the Assistant Director of the South West Academy of Nanoelectronics at the University of Texas at Austin. He has contributed to research on quantum computing, decoherence mechanisms in nanostructures, many-body theory, and quantum transport. He has authored more than 30 refereed publications and has given presentations at over 30 international conferences. His current research centers on spintronics, strongly correlated electron systems, and quantum transport theory.

Sanjay K. Banerjee (S'80–M'83–SM'89–F'96) received the B.Tech. degree from the Indian Institute of Technology (IIT), Kharagpur, India, in 1979, and the M.S. and Ph.D. degrees from the University of Illinois at Urbana–Champaign, in 1981 and 1983, respectively, all in electrical engineering.

He is the Cockrell Family Regents Chair Professor of Electrical and Computer Engineering and Director of the Microelectronics Research Center at the University of Texas at Austin. As a Member of Technical Staff, Corporate Research, Development and Engineering of Texas Instruments, Inc., from 1983–1987, he worked on polysilicon transistors and dynamic random access trench memory cells used by Texas Instruments in the world's first 4-Mb dynamic random access memory. He has been Assistant Professor (1987–1990), Associate Professor (1990–1993), and Professor (since 1993) with The University of Texas at Austin. He is currently active in the areas of ultrahigh vacuum and remote plasma-enhanced chemical vapor deposition for silicon–germanium–carbon heterostructure MOSFETs and nanostructures. He is also interested in the areas of ultrashallow junction technology and semiconductor device modeling. He has over 580 archival refereed publications/talks, seven books/chapters, and 26 U.S. patents. He has supervised over 40 Ph.D. and 50 M.S. students.

Dr. Banerjee was corecipient of the Best Paper Award, IEEE International Solid State Circuits Conference in 1986. He received the Engineering Foundation Advisory Council Halliburton Award in 1991, the Texas Atomic Energy Fellowship (1990–1997), Cullen Professorship (1997–2001), and the National Science Foundation Presidential Young Investigator Award in 1988. His recent awards include Fellow of APS (2006), Distinguished Alumnus Award, IIT (2005), Industrial R&D 100 Award (with Singh in 2004), Electro-Chemical Society (ECS) Callinan Award, 2003, IEEE Millennium Medal, 2000, and Semiconductor Research Corporation Inventor Recognition Award, 2000. He was a Distinguished Lecturer for IEEE Electron Devices Society and the General Chair of the IEEE Device Research Conference, 2002.